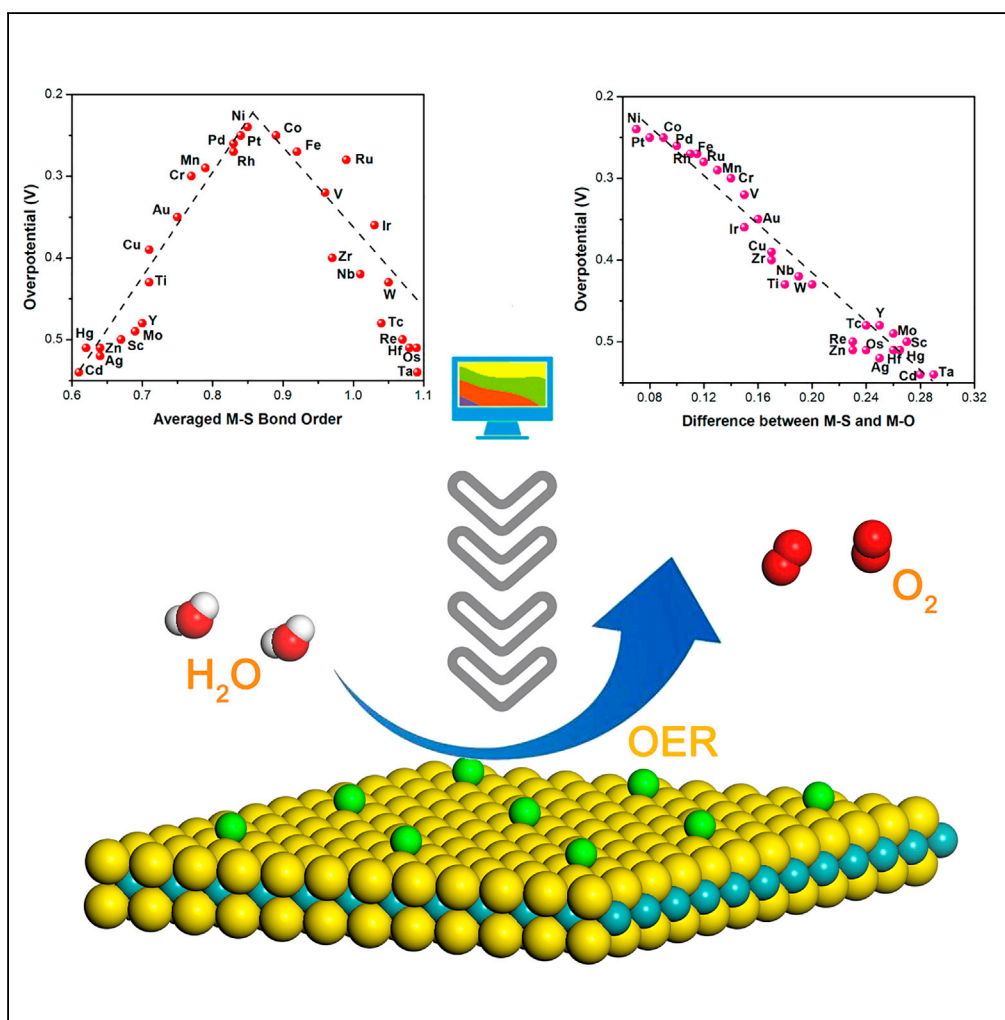


Article

Difference between Metal-S and Metal-O Bond Orders: A Descriptor of Oxygen Evolution Activity for Isolated Metal Atom-Doped MoS₂ Nanosheets



Guangtong Hai,
Hongyi Gao,
Guixia Zhao,
Wenjun Dong,
Xiubing Huang, Yi
Li, Ge Wang

guixiazhao@163.com (G.Z.)
gewang@mater.ustb.edu.cn
(G.W.)

HIGHLIGHTS

A predictive descriptor of OER activity for M-UMONs was proposed

Calculation and experiments were combined to explore the descriptor

A series of monatomic catalyst was prepared via a universal method

High-throughput calculation was applied to shorten the development cycle

Article

Difference between Metal-S and Metal-O Bond Orders: A Descriptor of Oxygen Evolution Activity for Isolated Metal Atom-Doped MoS₂ Nanosheets

Guangtong Hai,^{1,4} Hongyi Gao,^{1,4} Guixia Zhao,^{2,*} Wenjun Dong,¹ Xiubing Huang,¹ Yi Li,³ and Ge Wang^{1,5,*}

SUMMARY

Exploration of predictive descriptors for the performance of electrocatalytic oxygen evolution reaction (OER) is significant for material development in many energy conversion processes. In this work, we used high-throughput density functional theory (DFT) calculations to systematically investigate the OER performance of thirty kinds of isolated transition metal atoms-doped ultrathin MoS₂ nanosheets (M-UMONs). The results showed that the OER activity could be a function of the decorated transition metal-sulfur (M-S) bond orders with a volcanic-shaped correlation, and a strong correlation could be found when the difference of the M-S bond orders and corresponding metal-oxygen (M-O) bond orders were taken into consideration, implying that the difference in M-S and M-O bond orders could be a predictive descriptor of OER activity for M-UMON system. This successful result also implies this calculation-based method for the exploring of descriptors would also provide a new promising avenue for the discovery of high-performance OER catalysts.

INTRODUCTION

The design of high-performance catalysts for energy conversion and storage is a high priority in light of the popular pursuit of sustainable energy (Bergmann et al., 2018; Chia and Pumera, 2018; Gray, 2009; Kim et al., 2018; Roger et al., 2017). As a critical process, oxygen evolution reaction (OER) is usually the rate-limiting step for such energy conversions since the kinetics of OER are often unsatisfactory due to the four-electron transfer process, which usually requires a large overpotential to drive the reaction (Lewis and Nocera, 2006; Kanan and Nocera, 2008; Han et al., 2018; Silva et al., 2018; Wang et al., 2018a, 2018b; Liu et al., 2018a, 2018b). As a result, the large overpotential ineluctably results in low efficiency. Over the past few years, reports show that different noble-metal-based catalysts have been found to significantly reduce the overpotential of OER. However, these reported noble-metal based catalysts have been limited in their practical applicability owing to their high cost, which hinders the development of energy conversion devices (Xie et al., 2018; Chen et al., 2018; Yu et al., 2018; Guo et al., 2018).

An ideal catalyst should possess both high activity and low cost. For this purpose, a great deal of research has been performed to seek highly active materials based on earth-abundant elements. Recently, supported monatomic catalysts have drawn increasing attention because of their high utilization of active sites and the resulting high performance of the OER (Li et al., 2018; Fei et al., 2018; Yan et al., 2018; Chen et al., 2017) and have been considered as promising alternative electrocatalysts for the OER. However, how to rapidly obtain these desired monatomic OER catalysts without tedious “trial and error” remains a problem. An easily obtainable descriptor is urgently required for the rapid screening of desirable high-performance materials (Huang et al., 2017; Jacobs et al., 2018; Wang et al., 2018a, 2018b; Lin et al., 2017; Fang et al., 2017; Gu et al., 2018). By means of a descriptor, we can rapidly evaluate OER activity since obtaining the descriptor value is usually much faster than calculating the Gibbs free energy via frequency calculations. This method would significantly shorten the calculation time and thus reduce the calculation cost. Before experimentally preparing the catalysts, we can first screen out the desired materials quickly based on the descriptor, avoiding tedious trial and error and improve research efficiency. Hence, we seek to better understand the correlation between electrochemical performance and chemical structure by means of high-throughput density functional theory (DFT) calculations owing to their successful applications in material screening and then obtain a credible descriptor of OER activity for surface monatomic materials to predict and design highly active monatomic catalysts, that is, the metal atoms-doped ultrathin MoS₂ nanosheets (M-UMONs)

¹Beijing Advanced Innovation Center for Materials Genome Engineering, Beijing Key Laboratory of Function Materials for Molecule & Structure Construction, College of Materials Science and Engineering, University of Science and Technology Beijing, Xueyuan Street 30, Beijing, China

²Laboratory of Industrial Chemistry, Faculty of Chemistry and Biochemistry, Ruhr-Universität Bochum, Universitätsstraße 150, Bochum 44780, Germany

³State Key Laboratory of Inorganic Synthesis and Preparative Chemistry and International Center of Future Science, College of Chemistry, Jilin University, Qianjin Street, Changchun 2699, China

⁴These authors contributed equally

⁵Lead Contact

*Correspondence: guixiazhao@163.com (G.Z.), gewang@mater.ustb.edu.cn (G.W.)

<https://doi.org/10.1016/j.isci.2019.10.001>



detailed in this work. Fortunately, previously reported research provides us with a good reference. For examples, surface oxygen binding energy (Rossmeisl et al., 2007; Man et al., 2011), the enthalpy of a lower to higher oxide transition (Trasatti, 1980), and the 3d electron number (Bockris and Otagawa, 1984) are reported as successful OER activity descriptors. Although these proposed descriptors are not straightforward in their practical application (Suntivich et al., 2011a, 2011b), their exploration method and processes offer us much inspiration.

In this work, the credibility of our calculations of theoretical overpotentials was first validated when we explored the descriptor based on the DFT calculations. For the validation purpose, more than ten kinds of M-UMONs were prepared and systematically characterized, and the electrochemical experimental results confirmed our calculations. Based on this, different kinds of M-UMONs were theoretically investigated by means of using high-throughput DFT calculations. Our calculation results demonstrated a volcano-shaped correlation between the activity and metal-sulfur (M-S) bond orders. As the differences between the M-S bond orders and corresponding metal-oxygen (M-O) bond orders increased, the OER performance would decline, meaning that peak activity is predicted to occur when the bond order difference is minimal. More importantly, this successful exploration of the descriptor of OER performance for M-UMONs systems implies this calculation-based method for the exploring of descriptors would provide new promising avenues of research for the development of high-performance OER catalysts.

RESULTS AND DISCUSSION

Exploring descriptors usually requires a significant amount of data points to ensure the accuracy and reliability of the results. Using more traditional methods, data points are obtained from experimental results, requiring a huge quantity of synthesis and measurement procedures, which are time and resource consuming. A more efficient way of exploring descriptors is urgently desired. The emergence of high-throughput calculations offers an opportunity for solving this problem, which can rapidly generate a large number of credible data such as overpotentials that can be measured experimentally, as well as gathering electronic structure parameters that are difficult to obtain experimentally.

Before using high-throughput calculations, a reasonable initial model structure was constructed, so a series of pre-calculations could be performed on eleven kinds of M-UMONs, to identify the binding configurations (Figure S1 and Table S1), frontier orbitals calculations (Figure S2), electrostatic potential (ESP) distribution calculations (Figures S3 and S4), and adsorption energy calculations (Figure S5). These pre-calculations showed that the Mo-top binding configuration is energetically preferred and the activity mainly comes from the surface metal atoms, which agree with previous reports (Liu et al., 2017). For verification purposes, the eleven kinds of M-UMONs were prepared and systematically characterized using powder X-ray diffraction (Figure S6), transmission electron microscopy (Figure S7), atomic force microscopy (Figure S8), inductively coupled plasma-mass spectrometry (ICP-MS) (Table S2), and high-angle annular dark field-scanning transmission electron microscopy (HAADF-STEM) (Figure 1). These measurements highlight the successful preparation of the different M-UMONs, so the experimental data for these samples are credible. Additionally, the Mo-top binding configurations were experimentally observed in the HAADF-STEM images (Figure 1), in which the Mo atoms are distributed in a hexagonal pattern, and the supported transition metal atoms are located at the Mo-top sites, experimentally confirming the calculation results. In addition, no obvious aggregation was observed, verifying the atomic dispersion of the transition metal atoms. Collectively, the aforementioned results confirmed that the Mo-top binding configuration is the most stable and the activity is mainly from the surface metal atoms. Based on these results, all the subsequent calculations were based on the surface metal sites with Mo-top binding configuration.

In this work, the OER performance was appraised according to the overpotential since it is the key parameter for evaluating activity (Hai et al., 2018), and high-throughput DFT calculations were used to obtain the theoretical overpotentials for the subsequent exploration of the descriptors for OER performance. It should be noted that our calculated theoretical overpotentials results were first validated by the electrochemical measurements of the aforementioned eleven kinds of M-UMONs before using high-throughput calculations (Figures S9 and S10); thus, the use of the calculated theoretical overpotentials to explore the descriptors is a valid method. Since the substrate MoS₂ is a kind of 2D ultrathin nanosheet, the activity may also come from the edge sites (Friebe et al., 2015), so pure MoS₂ nanosheets

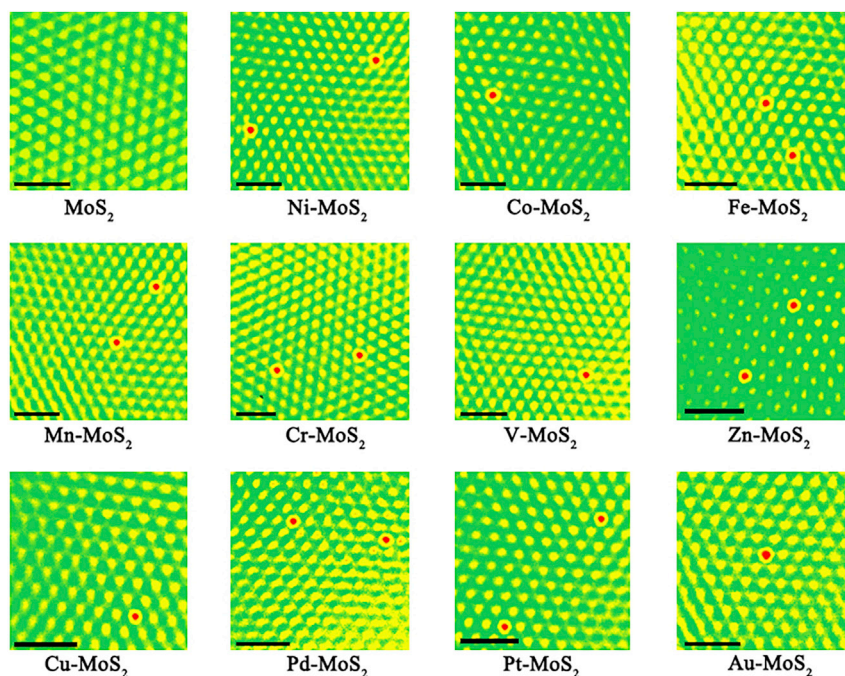


Figure 1. HAADF-STEM Images of the (002) Planes for Different M-UMONs and MoS₂ Ultrathin Nanosheets

The red color represents transition metal atoms supported on Mo-top sites, yellow for Mo atoms, and green for S atoms and the background. Scale bar, 1.0 nm. Since the contrast of atom columns is approximately proportional to the square of the atomic number in HAADF-STEM images, only the heavy transition metal atoms, namely, the Mo atoms and supported transition metal atoms, are visible as bright spots.

were also tested, and their negligible OER activity indicated that the OER activity of different M-UMONs are mainly the result of supported single metal atoms. The DFT calculation results of theoretical overpotentials represented by η are shown in Figure 2. (See theoretical calculations in [Supplemental Information](#)). As shown, the overpotentials for the M-UMONs decorated with transition metal elements in VIII group, such as Ni, Fe, and Co, are lower than that of the others and therefore could offer better performance. This result agrees well with the fact that proposed catalysts constructed based on VIII group transition metal elements have better performance toward OER compared with other transition metal elements-based materials (Gao et al., 2014; Liu et al., 2018a, 2018b; Roy et al., 2018). Meanwhile, in each period, the activity first increases until reaching the maximum at the VIII group and then drops again in relation to the rising of the atomic number of supported transition metal atoms. This apparent pattern implies that an inflection point exists in the position of the VIII group, which inspired us to investigate the correlation within the data to find a straightforward descriptor.

To investigate the activity-structure relationship for the M-UMONs system and then obtain a straightforward descriptor, a series of correlation analyses was conducted. To fully account for all kinds of possible descriptors, the local density of states (LDOS), electronic localization function (ELF), energy level of d-bands edges at the surface metal sites, deformation electron density, Fermi level, bond strength, and atomic charge were all taken into consideration and then empirically analyzed by rational inference, as detailed later. According to previous reports the specific structure of the M-UMONs and the OER processes (i.e., the active sites are the isolated metal atoms and the OH* bonded with these surface metal sites), the bond orders that are associated with the surface metal sites, the atomic charge at the surface metal sites, and certain d-band electronic structure parameters show greater promise of becoming the desired descriptors compared with other indexes (Hossain et al., 2019), that is to say, LDOS and ELF could neither accurately reflect the interaction between substrates and surface metal sites nor show the deformation electron density since it could only show the difference of electron density before and after bonding. Based on this, our correlation with theoretical overpotentials analysis mainly focuses on these screened possible descriptors, including bond population calculations, charge population calculations, and a series of electronic configuration parameters such as d-band edge and d-band electron number.

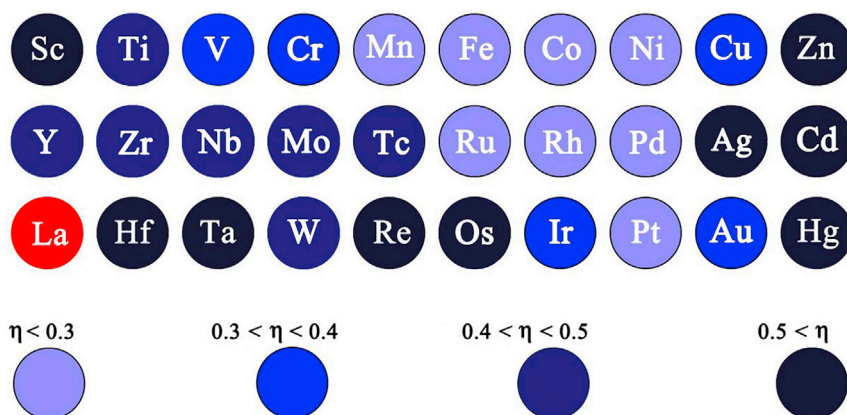


Figure 2. The High-throughput DFT Calculated Theoretical Overpotentials of Different Transition Metal-Based M-UMONs

Lanthanide series were not calculated in this work (red color). Unit: V.

The d-band center, d-band edge position, etc. were subsequently ruled out as descriptors as they are tedious in application (Suntivich et al., 2011a, 2011b). The atomic charge was also ruled out owing to its weak correlation with the theoretical overpotential as according to our calculation results, namely, more positive charges at the active sites do not necessarily result in better performance, even though OER is an oxidation reaction. The bond orders that are associated with the active sites, which could reflect the interaction strength between the active sites and MoS₂ supporter or reaction substrate, were expected to give a proper description of the OER performance (Hossain et al., 2019). This was subsequently confirmed by our bond population analysis, as shown in Figure 3. The distribution of M-S bond orders is similar to that of the theoretical overpotentials (Figure 2), that is, in each period, the M-S bond orders always possess a certain value (~ 0.85) at the VIII group, at which the corresponding M-UMONs offer the smallest theoretical overpotential. It can also be seen that the theoretical overpotentials would go higher with the deviation of M-S bond orders from the value at the VIII group, whenever the bond orders increase or decline. This result agrees well with the well-known Sabatier principles, in which a proper bond strength is required to achieve higher activity. It also should be noted that the bond order in this work was the Mayer bond order due to its transferability for different basis sets (Table S3). More specially, the Mayer bond order is defined below:

$$B_{AB} = 2 \sum_{\mu \in A} \sum_{\nu \in B} [(P^{\alpha} S)_{\mu\nu} (P^{\alpha} S)_{\nu\mu} + (P^{\beta} S)_{\mu\nu} (P^{\beta} S)_{\nu\mu}]$$

Here, B_{AB} is the bond orders between atom A and atom B and P^{α} , P^{β} are the density matrices for spin α and β . The bond order value could be directly obtained from the population analysis.

Collectively, the above-mentioned results indicated that the more the M-S bond orders deviate from this value, the higher the theoretical overpotentials would be. This result indicates the volcanic-shaped correlation between the OER activity and the M-S bond orders, and the peak activity should be located at a certain value.

To investigate this relationship, the correlation between M-S bond orders and theoretical overpotentials was further analyzed. As shown in Figure 4A, the theoretical overpotential of different M-UMONs is a volcanic-shaped function of the M-S bond orders, where the OER activities are compared through the theoretical overpotential to trigger the reaction. The volcanic-shaped activity trend might be explained as follows. The surface-supported transition metal atoms participate in the σ -bonding with both adsorbates (M-O bond) and sulfur atoms (M-S bond) during the OER processes, so the M-S bond strength could greatly influence the binding strength of the intermediates and thus the activity (Suntivich et al., 2011a, 2011b; Liu et al., 2017). According to the data shown on the left branch of the volcano, the weaker M-S bond strength limited the OER performance owing to the relatively strong M-O bonding, which is unfavorable for the dissociation and desorption of the intermediates. The weaker M-S bond strength would become the bottleneck that restricted the electron transfer between the surface and the MoS₂ substrate. As for the right branch of the volcano, the M-S bond is too strong, which is

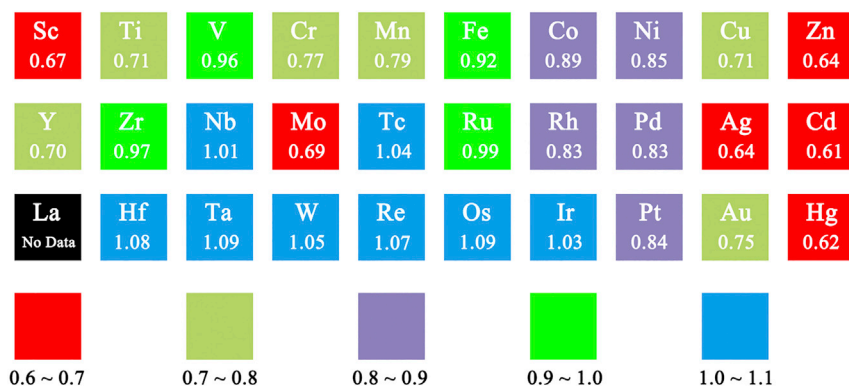


Figure 3. Averaged M-S Bond Orders of Different Kinds of M-UMONs

The averaged M-S bond orders values are displayed below the associated element symbol, and the attached boxes were mapped with different colors for different ranges.

unfavorable for the adsorption of the intermediates, and the weaker M-O bond strength would become the dominant factor restricting the electron transfer between the O^* and surface metal atoms. These results showed that the peak activity would occur when there is minimal difference between the M-S bond orders and M-O bond orders. Hence, further analysis was conducted from the perspective of the interaction of M-S and M-O bond orders with the theoretical overpotentials, and it was finally found that their differences were linearly correlated with the theoretical overpotentials. As shown in Figure 4B, an obvious linear decay of activity occurred as the difference between the M-S and M-O bond orders increased (see Figure S11 for M-O bond orders), confirming that the bond order difference can greatly impact the adsorption and influence the reaction's activity. Meanwhile, taking the bond order difference as the descriptor would be more credible. That is, for a specified kind of M-UMONs, the M-S and M-O bond orders were all derived from the same optimized structure and the same calculated parameters, and their difference, namely, the difference between M-S and M-O bond orders should reasonably make sense. Furthermore, in terms of the M-UMONs in the left branch, the G_4 value is the maximum value of the OER process, indicating that the potential determining step (PDS) is the deprotonation of OOH^* (Figure S12). Besides, the G_2 and G_5 values of the left branch are clearly higher than those of right branch, indicating that the weaker M-S bond is unfavorable for the dissociation and desorption of the intermediates. When it comes to the right branch, the G_3 value is the maximum value, demonstrating that the PDS is the adsorption of OH^- to form the O-O bond in OOH adsorbates. Also, the G_1 values of the right branch are significantly higher than those of the left branch, reflecting that the M-S bond that is too strong is unfavorable for the adsorption of the intermediates.

Our descriptor was intuitively validated by the electrochemical measurements of the aforementioned eleven kinds of M-UMONs. The experimental OER activity tendency experimentally confirmed the volcano-shaped correlation between the M-S bond order and the OER activity (Figure 4C). Additionally, these results also indicate that, as the M-S bond orders get closer to the M-O bond orders, this could enhance the OER activity (Figure 4D). Moreover, four kinds of M-UMONs were tested at the constant overpotential of 250 mV to evaluate their robustness. These results showed that the stability of M-UMONs during the OER process (Figure S13) has a positive correlation with the M-S bond orders, that is, a higher M-S bond order leads to better stability, which could be attributed to the more stable M-S bond with higher bond orders, preventing the loss of supported metal atoms. Even though only four samples were experimentally measured, their M-S bond orders were distributed at different ranges, which shows our results to be representative and credible. Besides, several kinds of M-UMONs, such as Ni-UMONs, Pt-UMONs, and Co-UMONs, could offer comparable OER performance or even outperform other commonly used OER catalysts, including Pt/C and RuO_2 (Figure S14). These results also confirmed that the construction of M-UMONs is a practical pathway to develop high-performance OER catalysts.

In conclusion, this work suggests that the relationship between M-S bond orders and corresponding M-O bond orders could significantly influence the OER activity for the M-UMONs system, and systematic investigations confirmed that their difference is a credible descriptor of OER activity for M-UMONs. Decreasing the bond order difference between M-S and M-O for enhancing the activity of M-UMONs materials is a

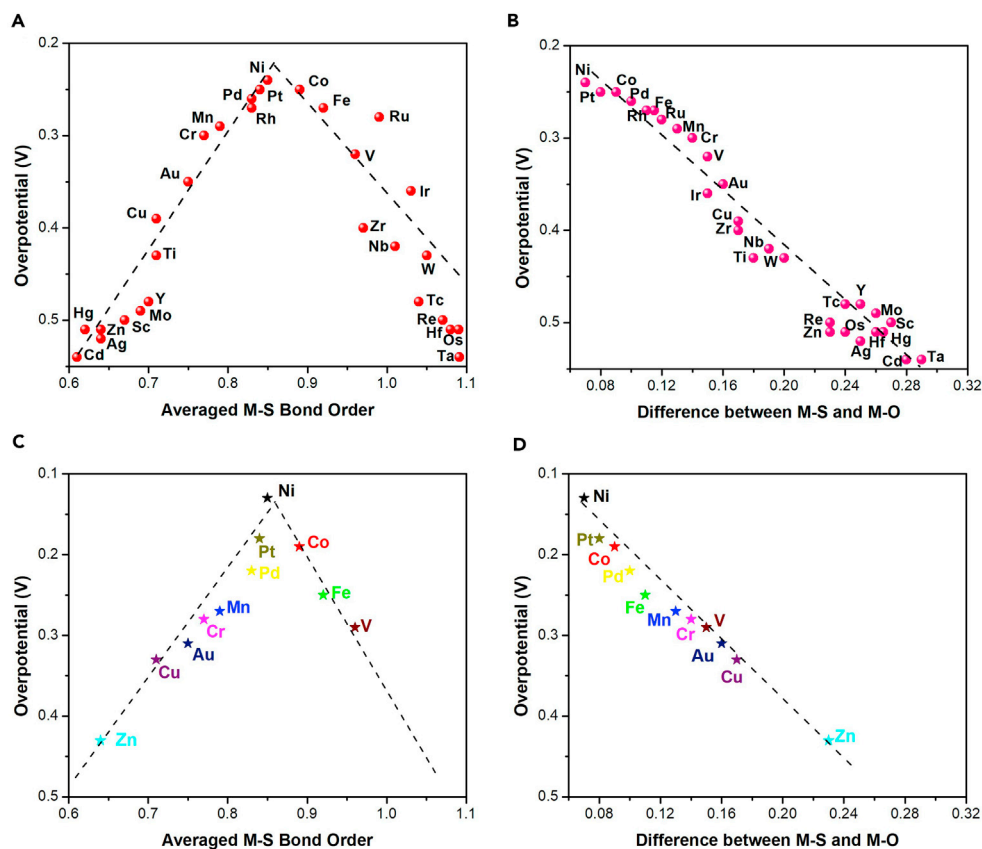


Figure 4. The Correlation between Bond Orders and Calculated Overpotential and Experimental Overpotential

(A) The relation between the theoretical overpotentials and averaged M-S bond orders.

(B) The correlation between the theoretical overpotentials and the difference between M-S and M-O bond orders.

(C) Experimental observed relations between the OER activity, defined by the onset overpotential at the current density of 5.0 mA cm^{-2} , and the averaged M-S bond orders.

(D) Experimental correlation between the OER activity and the difference between the M-S and M-O bond orders. The black dashed lines are for reference only.

promising strategy to create high-performance electrochemical catalysts for developing high-efficiency energy conversion devices. Furthermore, the successful practice in exploring the descriptor of OER activity for M-UMONs materials demonstrated that the calculation-based method is a practical pathway to obtain a credible descriptor of OER performance for fast materials screening and designing.

Limitation of the Study

The descriptor is sufficiently validated only for the M-UMONs system, and further research is needed for other systems. So far, we have started the study of the transferability of the bond order descriptor for other host materials, and it would be reported in our next research.

METHODS

All methods can be found in the accompanying [Transparent Methods supplemental file](#).

DATA AND CODE AVAILABILITY

The crystal structure of molybdenum disulfide reported in this paper could be accessed from the Crystallography Open Database (COD, no. 1010993).

SUPPLEMENTAL INFORMATION

Supplemental Information can be found online at <https://doi.org/10.1016/j.isci.2019.10.001>.

ACKNOWLEDGMENTS

This work was supported by the National Key Research and Development Program of China (No. 2016YFB0701100), the National Natural Science Foundation of China (51702013), and the Fundamental Research Funds for the Central Universities (FRF-BD-18-013A). Not OER, United States.

AUTHOR CONTRIBUTIONS

G.H. designed the study. G.H. and X.H. carried out the sample synthesis and electrochemical measurements. G.H. and H.G. performed the electron microscopy characterization. G.H., G.Z., Y.L., and W.D. finished the DFT calculations and analysis. G.H., X.H., G.W., and G.Z. wrote the manuscript. G.H. conducted the AFM and ICP-MS measurements. W.D., G.Z., X.H., and G.W. reviewed the data and revised portions of the manuscript, triggering helpful discussions.

DECLARATION OF INTERESTS

The authors declare no competing interests.

Received: April 24, 2019

Revised: September 26, 2019

Accepted: September 30, 2019

Published: October 25, 2019

REFERENCES

- Bergmann, A., Jones, T.E., Moreno, E.M., Teschner, D., Chernev, P., Glied, M., Reier, T., Dau, H., and Strasser, P. (2018). Unified structural motifs of the catalytically active state of Co(oxyhydr)oxides during the electrochemical oxygen evolution reaction. *Nat. Catal.* 1, 711–719.
- Bockris, J.O.'M., and Otagawa, T. (1984). The electrocatalysis of oxygen evolution on perovskites. *J. Electrochem. Soc.* 131, 290–302.
- Chen, Z., Mitchell, S., Vorobyeva, E., Leary, R.K., Hauert, R., Furnival, T., Ramasse, Q.M., Thomas, J.M., Midgley, P.A., Dontsova, D., et al. (2017). Stabilization of single metal atoms on graphitic carbon nitride. *Adv. Funct. Mater.* 27, 1605785.
- Chen, D., Zhang, H., Li, Y., Pang, Y., Yin, Z., Sun, H., Zhang, L.-C., Wang, S., Saunders, M., Barker, E., and Jia, G. (2018). Spontaneous formation of noble- and heavy-metal-free alloyed semiconductor quantum rods for efficient photocatalysis. *Adv. Mater.* 30, 1803351.
- Chia, X., and Pumera, M. (2018). Characteristics and performance of two-dimensional materials for electrocatalysis. *Nat. Catal.* 1, 909–921.
- Fang, M., Dong, G., Wei, R., and Ho, J.C. (2017). Hierarchical nanostructures: design for sustainable water splitting. *Adv. Energy Mater.* 7, 1700559.
- Fei, H., Dong, J., Feng, Y., Allen, C.S., Wan, C., Voloskiy, B., Li, M., Zhao, Z., Wang, Y., Sun, H., et al. (2018). General synthesis and definitive structural identification of MN_4C_4 single-atom catalysts with tunable electrocatalytic activities. *Nat. Catal.* 1, 63–72.
- Friebel, D., Louie, M.W., Bajdich, M., Sanwald, K.E., Cai, Y., Wise, A.M., Cheng, M.-J., Sokaras, D., Weng, T.-C., Alonso-Mori, R., et al. (2015). Identification of highly active Fe sites in (Ni,Fe) OOH for electrocatalytic water splitting. *J. Am. Chem. Soc.* 137, 1305–1313.
- Gao, M., Sheng, W., Zhuang, Z., Fang, Q., Gu, S., Jiang, J., and Yan, Y. (2014). Efficient water oxidation using nanostructured α -Nickel-hydroxide as an electrocatalyst. *J. Am. Chem. Soc.* 136, 7077–7084.
- Gray, H.B. (2009). Powering the planet with solar fuel. *Nat. Chem.* 1, 7.
- Gu, Z., Zhang, L., Wen, B., An, X., Lan, H., Liu, L.-M., Chen, T., Zhang, J., Cao, X., Tang, J., et al. (2018). Efficient design principle for interfacial charge separation in hydrogen-intercalated nonstoichiometric oxides. *Nano Energy* 53, 887–897.
- Guo, Y., Tang, J., Wang, Z., Kang, Y.-M., Bando, Y., and Yamauchi, Y. (2018). Elaborately assembled core-shell structured metal sulfides as a bifunctional catalyst for highly efficient electrochemical overall water splitting. *Nano Energy* 47, 494–502.
- Hai, G., Jia, X., Zhang, K., Liu, X., Wu, Z., and Wang, G. (2018). High-performance oxygen evolution catalyst using two-dimensional ultrathin metal-organic frameworks nanosheets. *Nano Energy* 44, 345–352.
- Han, X., Wu, X., Deng, Y., Liu, J., Lu, J., Zhong, C., and Hu, W. (2018). Ultrafine Pt nanoparticle-decorated pyrite-type CoS_2 nanosheet arrays coated on carbon cloth as a bifunctional electrode for overall water splitting. *Adv. Energy Mater.* 8, 1800935.
- Hossain, M.D., Liu, Z., Zhuang, M., Yan, X., Xu, G.-L., Gadre, C.A., Tyagi, A., Abidi, I.H., Sun, C.-J., Wong, H., et al. (2019). Rational design of graphene-supported single atom catalysts for hydrogen evolution reaction. *Adv. Energy Mater.* 9, 1803689.
- Huang, Z.-F., Wang, J., Peng, Y., Jung, C.-Y., Fisher, A., and Wang, X. (2017). Design of efficient bifunctional oxygen reduction/evolution electrocatalyst: recent advances and perspectives. *Adv. Energy Mater.* 7, 1700544.
- Jacobs, R., Mayeshiba, T., Booske, J., and Morgan, D. (2018). Material discovery and design principles for stable, high activity perovskite cathodes for solid oxide fuel cells. *Adv. Energy Mater.* 8, 1702708.
- Kanan, M.W., and Nocera, D.G. (2008). In situ formation of an oxygen-evolving catalyst in neutral water containing phosphate and Co^{2+} . *Science* 321, 1072–1075.
- Kim, N., Sa, Y.J., Yoo, T.S., Choi, S.R., Afzal, R.A., Choi, T., Seo, Y.-S., Lee, K.-S., Hwang, J.Y., Choi, W.S., et al. (2018). Oxygen-deficient triple perovskites as highly active and durable bifunctional electrocatalysts for oxygen electrode reactions. *Sci. Adv.* 4, eaap9360.
- Lewis, N.S., and Nocera, D.G. (2006). Powering the planet: chemical challenges in solar energy utilization. *Proc. Natl. Acad. Sci. U S A* 103, 15729–15735.
- Li, G., Zhang, Y.-Y., Guo, H., Huang, L., Lu, H., Lin, X., Wang, Y.-L., Du, S., and Gao, H.-J. (2018). Epitaxial growth and physical properties of 2D materials beyond graphene: from monatomic materials to binary compounds. *Chem. Soc. Rev.* 47, 6073–6100.
- Lin, C.-Y., Zhang, L., Zhao, Z., and Xia, Z. (2017). Design principles for covalent organic frameworks as efficient electrocatalysts in clean energy conversion and green oxidizer production. *Adv. Mater.* 29, 1606635.
- Liu, G., Robertson, A.W., Li, M.M.-J., Kuo, W.C.H., Darby, M.T., Muhieddine, M.H., Lin, Y.-C., Suenaga, K., Stamatakis, M., Warner, J.H., and Tsang, S.C.E. (2017). MoS_2 monolayer catalyst doped with isolated Co atoms for the hydrodeoxygenation reaction. *Nat. Chem.* 9, 810–816.

Liu, L., Su, H., Tang, F., Zhao, X., and Liu, Q. (2018a). Confined organometallic Au_1N_x single-site as an efficient bifunctional oxygen electrocatalyst. *Nano Energy* 46, 110–116.

Liu, K., Zhang, C., Sun, Y., Zhang, G., Shen, X., Zou, F., Zhang, H., Wu, Z., Wegener, E.C., Taubert, C.J., et al. (2018b). High-performance transition metal phosphide alloy catalyst for oxygen evolution reaction. *ACS Nano* 12, 158–167.

Man, I.C., Su, H.-Y., Calle-Vallejo, F., Hansen, H.A., Martinez, J.I., Inoglu, N.G., Kitchin, J., Jaramillo, T.F., Nørskov, J.K., and Rossmeisl, J. (2011). Universality in oxygen evolution electrocatalysis on oxide surfaces. *ChemCatChem* 3, 1159–1165.

Roger, I., Shipman, M.A., and Symes, M.D. (2017). Earth-abundant catalysts for electrochemical and photoelectrochemical water splitting. *Nat. Rev. Chem.* 1, 0003.

Rossmeisl, J., Qu, Z.-W., Zhu, H., Kroes, G.-J., and Nørskov, J.K. (2007). Electrolysis of water on oxide surfaces. *J. Electroanal. Chem.* 607, 83–89.

Roy, C., Sebok, B., Scott, S.B., Fiordaliso, E.M., Sørensen, J.E., Bodin, A., Trimarco, D.B., Damsgaard, C.D., Vesborg, P.C.K., Hansen, O., et al. (2018). Impact of nanoparticle size and lattice oxygen on water oxidation on $NiFeO_xH_y$. *Nat. Catal.* 1, 820–829.

Silva, G.C., Fernandes, M.R., and Ticianelli, E.A. (2018). Activity and stability of Pt/IrO₂ bifunctional materials as catalysts for the oxygen evolution/reduction reactions. *ACS Catal.* 8, 2081–2092.

Suntivich, J., Gasteiger, H.A., Yabuuchi, N., Nakanishi, H., Goodenough, J.B., and Yang, S.-H. (2011a). Design principles for oxygen-reduction activity on perovskite oxide catalysts for fuel cells and metal–air batteries. *Nat. Chem.* 3, 546–550.

Suntivich, J., May, K.J., Gasteiger, H.A., Goodenough, J.B., and Yang, S.-H. (2011b). A perovskite oxide optimized for oxygen evolution catalysis from molecular orbital principles. *Science* 334, 1383–1385.

Trasatti, S. (1980). Electrocatalysis by oxides—attempt at a unifying approach. *J. Electroanal. Chem.* 111, 125–131.

Wang, D., Sheng, T., Chen, J., Wang, H.-F., and Hu, P. (2018a). Identifying the key obstacle in photocatalytic oxygen evolution on rutile TiO₂. *Nat. Catal.* 1, 291–299.

Wang, H.-F., Tang, C., and Zhang, Q. (2018b). A review of precious-metal-free bifunctional oxygen electrocatalysts: rational design and applications in Zn–air batteries. *Adv. Funct. Mater.* 28, 1803329.

Xie, M., Xiong, X., Yang, L., Shi, X., Asiri, A.M., and Sun, X. (2018). An Fe(TCNQ)₂ nanowire array on Fe foil: an efficient non-noble-metal catalyst for the oxygen evolution reaction in alkaline media. *Chem. Commun. (Camb.)* 54, 2300–2303.

Yan, H., Zhao, X., Guo, N., Lyu, Z., Du, Y., Xi, S., Guo, R., Chen, C., Chen, Z., Liu, W., et al. (2018). Atomic engineering of high-density isolated Co atoms on graphene with proximal-atom controlled reaction selectivity. *Nat. Commun.* 9, 3197.

Yu, F., Zhou, H., Huang, Y., Sun, J., Qin, F., Bao, J., Goddard, W.A., III, Chen, S., and Ren, Z. (2018). High-performance bifunctional porous non-noble metal phosphide catalyst for overall water splitting. *Nat. Commun.* 9, 9551.

ISCI, Volume 20

Supplemental Information

Difference between Metal-S and Metal-O Bond

Orders: A Descriptor of Oxygen Evolution Activity for

Isolated Metal Atom-Doped MoS₂ Nanosheets

Guangtong Hai, Hongyi Gao, Guixia Zhao, Wenjun Dong, Xiubing Huang, Yi Li, and Ge Wang

iScience

Supplemental Information

Difference between Metal-S and Metal-O bond order: A descriptor of oxygen evolution performance for isolated metal atom-doped MoS₂ nanosheets

Guangtong Hai, Hongyi Gao, Guixia Zhao, Wenjun Dong, Xiubing Huang, Yi Li, and

Ge Wang

Transparent Methods

Theoretical calculations

All the spin-polarized calculations were based on the density functional theory (DFT) with the combination of atomic orbitals (LCAO) method. The general gradient approximation (GGA) was used throughout with the revised Perdew-Burke-Ernzerhof (RPBE) parametrized exchange-correlation functional. Besides, a polarized basis set of double numerical plus polarization was employed to expand the wavefunction with a fine integration grid during the calculations. To obtain an accurate result, a large orbital cutoff of 6.5 Å was applied, and the relativistic effect of heavy metal atoms was treated using DFT semi-core pseudopotentials core treatment method to describe the electron-ion interaction.

All the model structures were built with Mo-top binding configuration on plane (002). The desired surface was modeled with two MoS₂ layers, which is consistent with the atomic force microscope (AFM) results. A sufficient large vacuum slab of 15 Å was used to eliminate the interactions between MoS₂ layers and the dipole correction was applied along the surface normal vector.

During the geometry optimizations, all the atoms were relaxed and optimized to the ground state with no imaginary frequency. To obtain the energy of the ground state exactly, the magnetic state of transition metal atoms including high and low spin state were considered, and the lowest energy structure was used as the ground state. Specially, the basis set superposition error (BSSE) correction was applied for a credible adsorption energy with M-UMONs specified to Counterpoise1 and adsorbed *OH specified to Counterpoise 2. To improve the computational efficiency, the delocalized internal coordinate was applied. Here, the surface cell was extended to a (4 × 4 × 1) supercell due to the mass loading of single atoms is usually below 10 %, and this model was basically consistent to subsequent atomic percentage results derived from the ICP-MS results shown in Table. S2. The (5 × 5 × 1) k-point grid was used for Brillouin-zone integrations. The O₂ and H₂O molecules

were optimized in a $(10 \times 10 \times 10) \text{ \AA}^3$ box with a Gamma point only k-point set. The convergence criteria was 10^{-7} for self-consistent field calculations, the model structures were optimized until the max force is below 0.003 Ha/ \AA and energy change is below 10^{-5} Hartree. Furthermore, the conductor-like screening model was used to describe the solvation effects, and the dielectric constant of solvent (water) was set to 78.54.

According to the frontier orbitals and electrostatic potential (ESP) calculations, we proposed that the surface transitional metal sites are the main active sites, so the reaction mechanism calculations were based on these metal sites. A fine grid with the interval of 0.15 \AA was applied in the ESP calculations. The k-point set is $(5 \times 5 \times 1)$ for the ESP calculations and Gamma point only for orbitals calculations.

The thermodynamic properties were obtained from the frequency calculations. Besides, the bond population calculations were employed to obtain the M-S and M-O bond orders information. Because the Milliken bond orders are strongly depended on the choice of basis set, more transferable Mayer bond orders are applied here, which is suitable for describing similar molecules (Mayer, 1986). The definition of Mayer bond order was shown below:

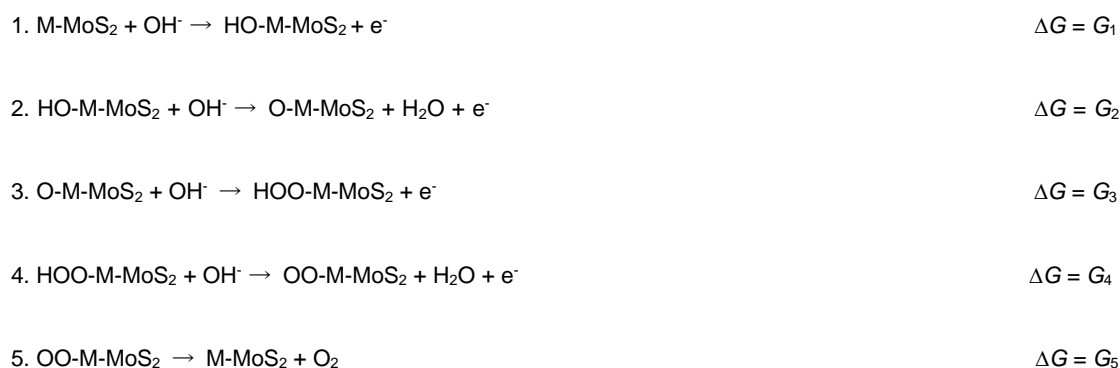
$$B_{AB} = 2 \sum_{\mu \in A} \sum_{v \in B} [(P^\alpha S)_{\mu v} (P^\alpha S)_{v \mu} + (P^\beta S)_{\mu v} (P^\beta S)_{v \mu}]$$

Here, B_{AB} is the bond orders between atom A and atom B. P^α , P^β are the density matrices for spin α and β . According to our test results shown below, when the basis set was changed, the Mayer bond orders was almost unchanged, which is transferable for different basis sets.

In Mo-top binding configuration model structure, each surface transitional metal atom is coordinated with three S atoms (MS_3 coordinate units), and these three M-S bond order values are unequal, so the averaged value is applied to estimate the bond orders. According to our test, the M-S and M-O bond orders values in different OER steps are also variable, but the differences are very small, so the same values in adsorption

configurations of step 1 were applied for simplicity, that is, the M-S and M-O bond orders were all derived from the “HO-M-MoS₂” configuration in step 1.

As for the theoretical overpotential (denoted as η) calculations, four-electron sequent transport mechanism was applied. As shown below, the Gibbs free energy change for four steps was denoted as G_1 , G_2 , G_3 , G_4 and G_5 , respectively.



The Gibbs free energy change could be transformed to the potential through the formula below:

$$E (\text{vs. SHE}) = -(-\Delta G - \Delta G^{\text{SHE}}) / nF$$

Here, ΔG is the Gibbs free energy change, and the maximum ΔG value of G_1 , G_2 , G_3 , G_4 and G_5 should be used to calculate the theoretical overpotential, n is the number of moles of electrons in the reaction, F is Faraday constant (96485 C mol⁻¹), respectively. Since the OER is an oxidation reaction, the $-\Delta G$ values (the Gibbs free energy of corresponding reduction reaction) were applied to calculate the standard electrode potential. ΔG^{SHE} is the Gibbs free energy change of the reduction of the proton ($\text{H}^+ + \text{e}^- \rightarrow 1/2 \text{H}_2$), and we adopt the experimental value, $\Delta G^{\text{SHE}} = -418$ kJ/mol (Torres et al., 2011).

According to the Nernst equation, the potential of work electrode (vs. SHE) could be transformed to the potential versus reversible hydrogen electrode (RHE) by the formula: $E (\text{vs. RHE}) = E (\text{vs. SHE}) + 0.0592 \text{ pH}$.

The thermodynamic potential of OER ($E_0 \text{H}_2\text{O}/\text{O}_2 = 1.23$ V vs. RHE) is used as reference to obtain the theoretical

overpotential through the formula: $\eta = E \text{ (vs. RHE)} - 1.23 = E \text{ (vs. SHE)} + 0.0592 \text{ pH} - 1.23$. In this work, the theoretical overpotential calculations were based on the conditions of pH = 14 (alkaline condition).

In this work, all the possible descriptors were taken into consideration in data analysis. For easily production run, we were aimed to obtain a convenient linear correlation between the descriptor and the overpotential. Hence, all the data correlation analysis were based on the linear regression (LR) algorithms. Candidate descriptors that without linear correlation with overpotential were all ruled out to be applied as the final desired descriptor. After the analysis and screening, the difference between M-S and M-O bond orders were found to most strongly correlated with overpotential and then reasonably to be employed as the descriptor.

Preparation of different M-UMONs

1 mmol of hexaammonium heptamolybdate tetrahydrate (HHT) and 30 mmol of thiourea were dissolved in 35 mL water with vigorous stirring to obtain the uniform solution and then transferred to a 50 mL reaction kettle and maintained at 493 K for 20 h. Then the product was washed with water for three times and frozen drying. The obtained MoS₂ nanosheets were stored in an air tight test tube.

To obtain different kinds of M-UMONs, 0.05 mmol of associated transition metal salt, that is, nickel acetate tetrahydrate for Ni-UMONs, cobalt acetate tetrahydrate for Co-UMONs, copper acetate for Cu-UMONs, zinc acetate dihydrate for Zn-UMONs, manganese acetate tetrahydrate for Mn-UMONs, palladium acetate for Pd-UMONs, ferric(II) acetate tetrahydrate for Fe-UMONs, chloroauric acid for Au-UMONs, chloroplatinic acid hexahydrate for Pt-UMONs, vanadium dichloride for V-UMONs, chromium acetate for Cr-UMONs; and 18 mg of thiourea were added to 2 mL of mixed solution of water and ethanol, and then left overnight. Subsequently this mixed solution was added into 50 mL of 1 mg mL⁻¹ MoS₂ colloid (12 mL of isopropanol, 38 mL of water with 50 mg of polyvinylpyrrolidone (PVP)) with vigorous stirring for 30 min. The colloid was then transferred to a 100 mL reaction kettle, and maintained at 433 K for 24 h. After the hydrothermal treatment, the product was washed

three times using water and then frozen dried under vacuum for 6 h. To avoid the aggregation and self-nucleation of these transition metal atoms, very low concentration of associated transition metal saline solution was used in this work (Liu et al., 2017). Therefore, we repeated above procedures three times to achieve a desired mole number loading.

Electrochemical measurements

The electrochemical measurements were carried out through a Princeton PMC 1000 & 500 electrochemical workstation with a typical three-electrode configuration. The as-prepared M-UMONs were dispersed in a mixed solution of 0.5 mL ethanol, 0.03 mL 5 wt % Nafion solution. After ultrasonication for 30 min, the mixed solution was dropped on the glass-carbon electrode (GCE) uniformly, and then used as the working electrode. Here, we assumed that the OER activity was mainly from the supported transition metal atoms, based on this, the moles numbers of loaded transition metal atoms were all kept at 2.0 μmol for different kinds of M-UMONs to make the results comparable. The saturate calomel electrode was applied as reference electrode and a small platinum foil (1 cm \times 1 cm) worked as the counter electrode, respectively. To obtain a credible result, the LSV curves were recorded at a low scan rate of 5 mV s^{-1} , which is able to minimize the capacitive current (Stevens et al., 2017; Zhuang et al., 2014). The chronoamperometric test was performed at the overpotential of 0.25 V. In this work, we normalized the specific activity by the amount of active metal atoms. To make the comparison meaningful, the moles numbers of Ru atoms were also kept at 2.0 μmol , that is 2 μmol of RuO_2 (0.26 mg RuO_2) during the electrochemical measurements of RuO_2 . In addition, all the potentials were calibrated to RHE by the formula: $E_{\text{RHE}} = E_{\text{SCE}} + 0.24 + 0.0592 \text{ pH}$. The electrolyte used in this work was 1 M KOH (high-purity) solution and the impedance of 1 M KOH solution at ambient temperature was measured at about 9 Ω , and all the data were corrected with iR-compensation.

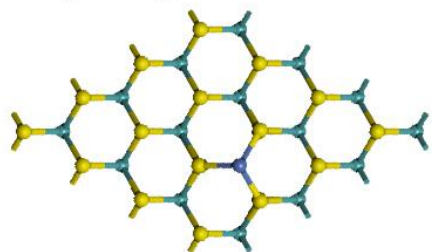
Characterizations

The high-angle annular dark field scanning transmission electron microscope (HAADF-STEM) image was recorded by an aberration-corrected transmission electron microscopy (Cs-corrected TEM) (FEI Titan 80-300).

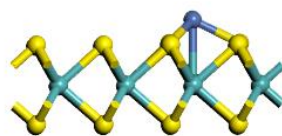
The TEM images were recorded by a field emission high resolution transmission electron microscopy (JEOL JEM-2010). The thickness of these sample was measured by an AFM (Shimadzu SPM-960). The crystal structures were defined by XRD (Bruke D8 Advance diffractometer, Cu K α 1). The ICP-MS was measured by the Agilent 7500ce system.

Supplemental Figures

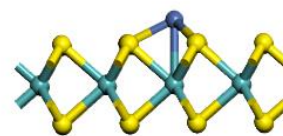
Mo-top binding



Top view

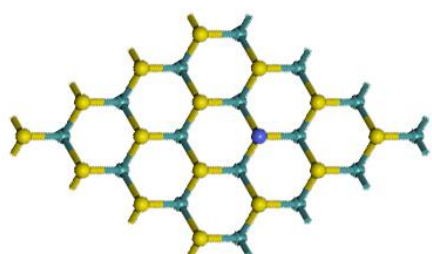


Side view

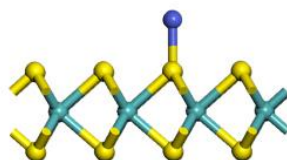


Side view

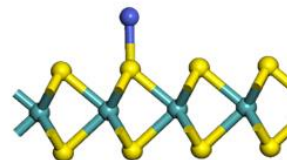
S-top site binding



Top view

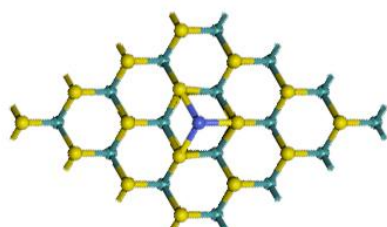


Side view

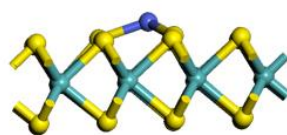


Side view

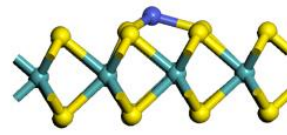
Cav site binding



Top view



Side view



Side view

Figure S1. Illustration of three possible binding configurations (Related to Figure 1). Colour scheme for elements: yellow for S, cyan for

Mo, blue for transition metal atoms.

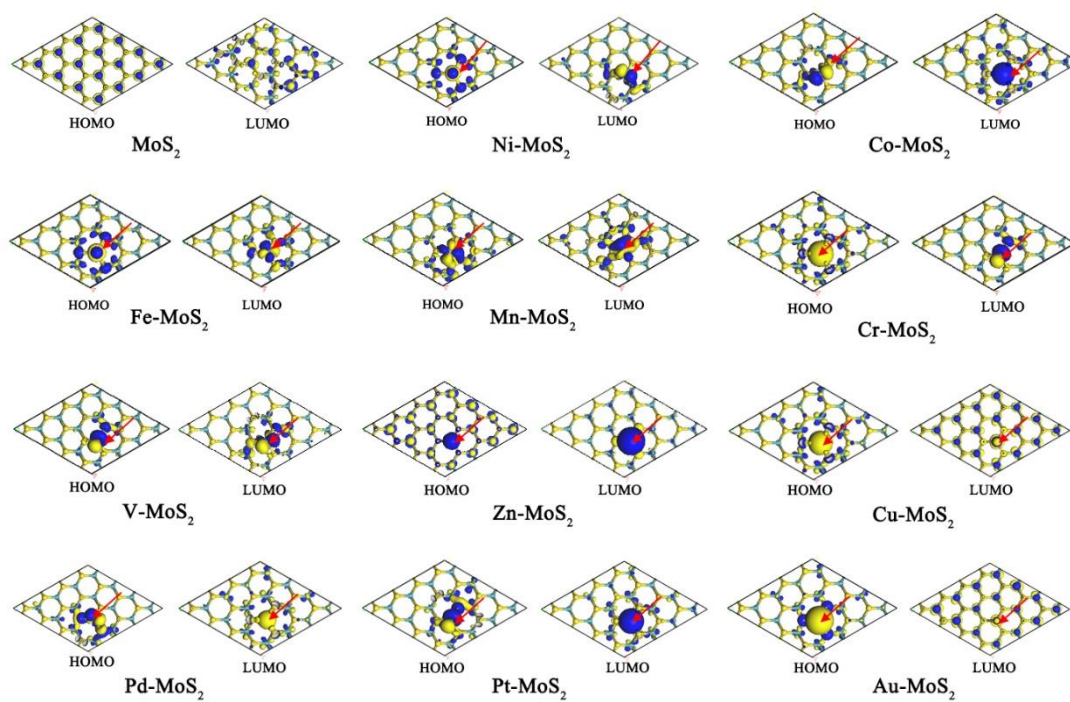


Figure S2. Spatial distribution of frontier orbitals (HOMO and LUMO) of different M-UMONs (Related to Figure 1). The red arrow indicates the surface transitional metal sites. These results showed the frontier orbital is intensively distributed at the surface metal sites, indicating these sites are the main active sites (Chattaraj et al., 2003).

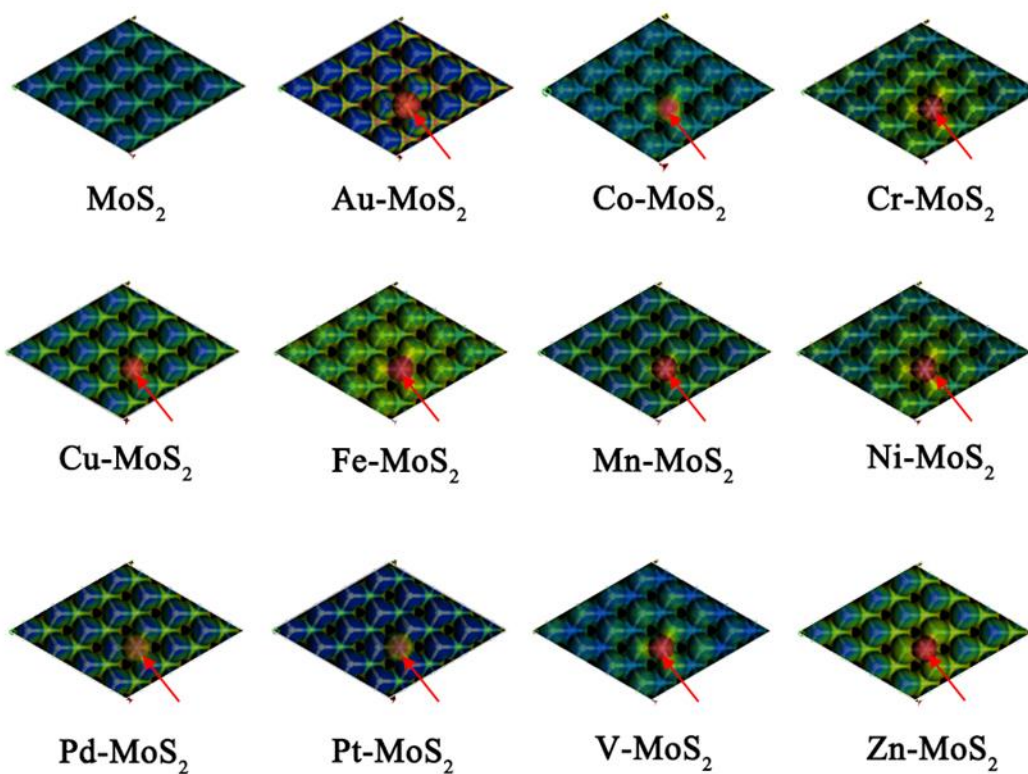


Figure S3. 3D electron density isovalue (isovalue = 0.2) surface mapped with ESP of different M-UMONs (the ESP value increases from blue to red) (Related to Figure 1). The red arrow indicates the surface transitional metal site. These results indicated the surface metal sites possess more positive ESP values, benefitting the adsorption of negative-charged OH^- .

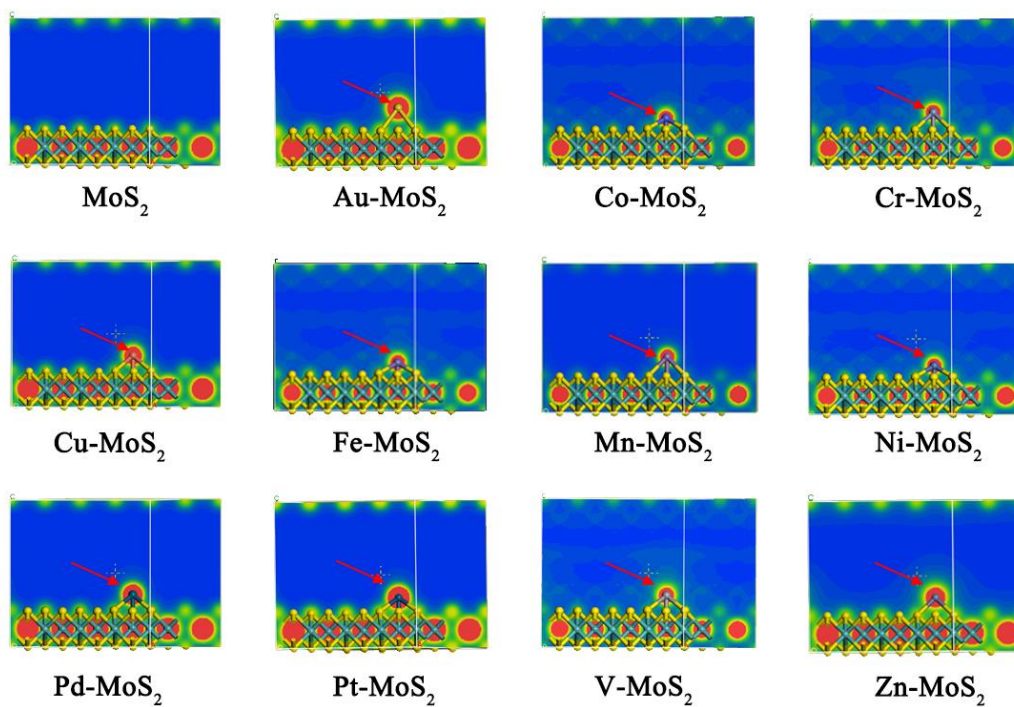


Figure S4. Sectional view of the ESP distribution (Related to Figure 1 and S3). The red arrow indicates the surface transitional metal site.

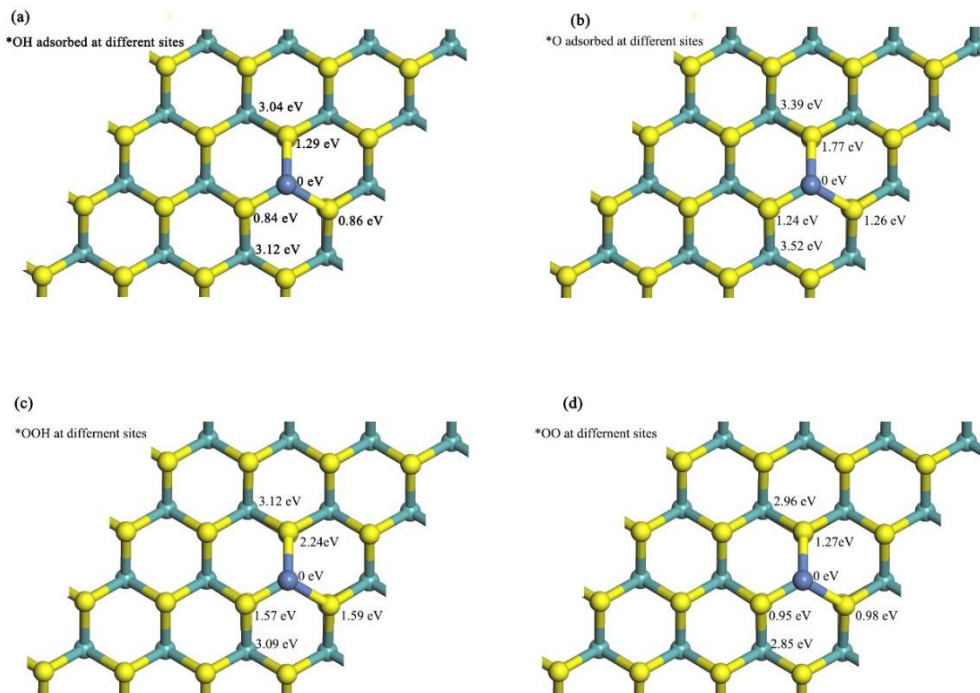


Figure S5. The adsorption energy of the OER intermediates at different surface sites of Ni-UMONs (Related to Figure 1). The value of

surface Ni atom site is used as reference. The adsorption energy was calculated used below formula:

$$E_{\text{ads}} = E(A+B) - E(A) - E(B) + E(\text{BSSE})$$

Here, the E_{ads} is the adsorption energy, $E(A+B)$ is the total energy of intermediates and Ni-UMONs after adsorption. $E(A)$ and $E(B)$

are the total energy of the intermediates and Ni-UMONs, respectively (Mavrikakis et al., 1998). Specially, the $E(\text{BSSE})$ is the BSSE

corrected energy and was calculated by the formula below:

$$E(\text{BSSE}) = [E(A) - E(A, \text{bAB})] + [(E(B) - E(B, \text{bAB}))]$$

Here, $E(A, \text{bAB})$ is the energy of A with the basis set of both A and B, $E(B, \text{bAB})$ is the energy of B with the basis set of A and B. As

shown above, the OER intermediates are energetically preferred to be adsorbed at surface metal sites. It should be noted that the basis

set superposition error (BSSE) was taken into consideration since the adsorption energy was calculated and derived from the LCAO

method.

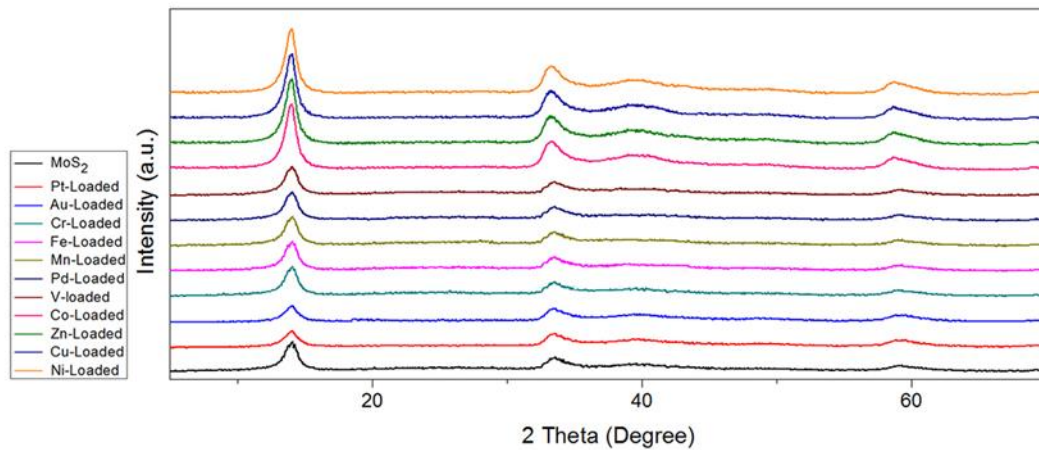


Figure S6. XRD patterns of MoS₂ nanosheets and different M-UMONs (Related to Figure 1). These results indicated that these M-UMONs share the same crystal structure with MoS₂ nanosheets, and no other peaks were detected, indicating the transition metal atoms were atomic dispersed on the surface of MoS₂. Besides, the strongest (002) diffraction peak in XRD patterns clarified plane (002) is the most exposed to the solution during OER process, proving that DFT calculations on plane (002) is rational.

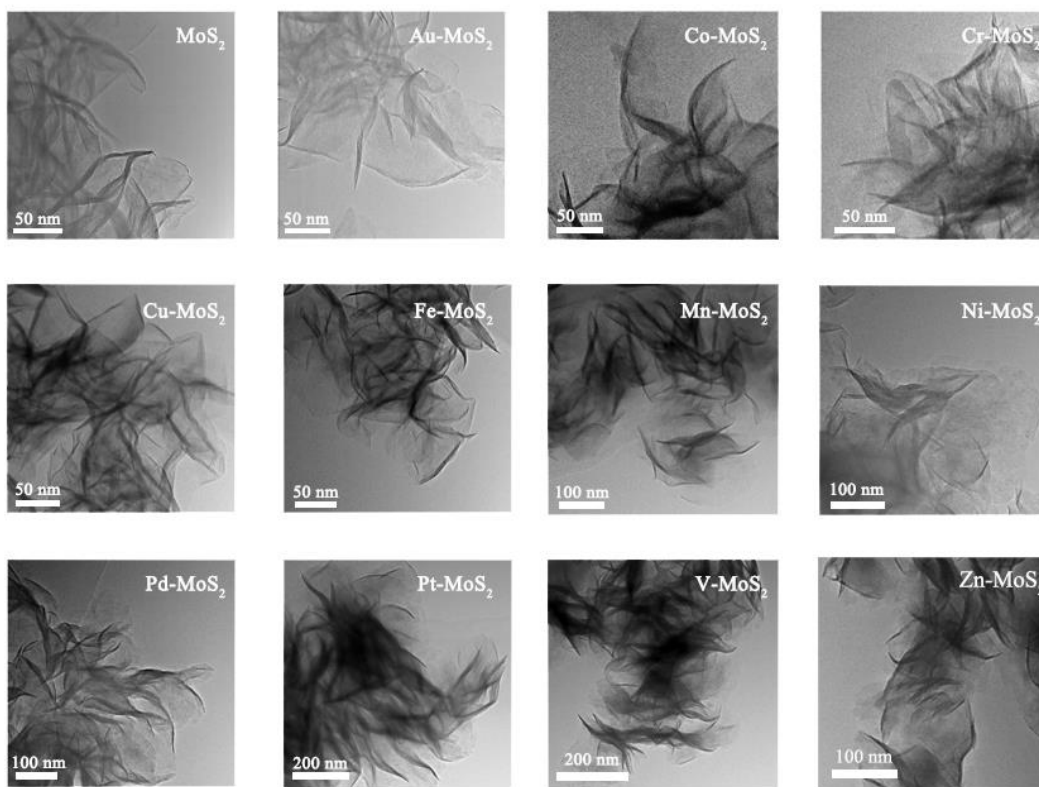


Figure S7. TEM images of different M-UMONs and MoS₂ nanosheets (Related to Figure 1). The TEM images indicate the M-UMONs have a 2D ultrathin morphology. Owing to the ultrathin flexible feature, the edges of the nanosheets curled spontaneously during drying (Zhao et al., 2016).

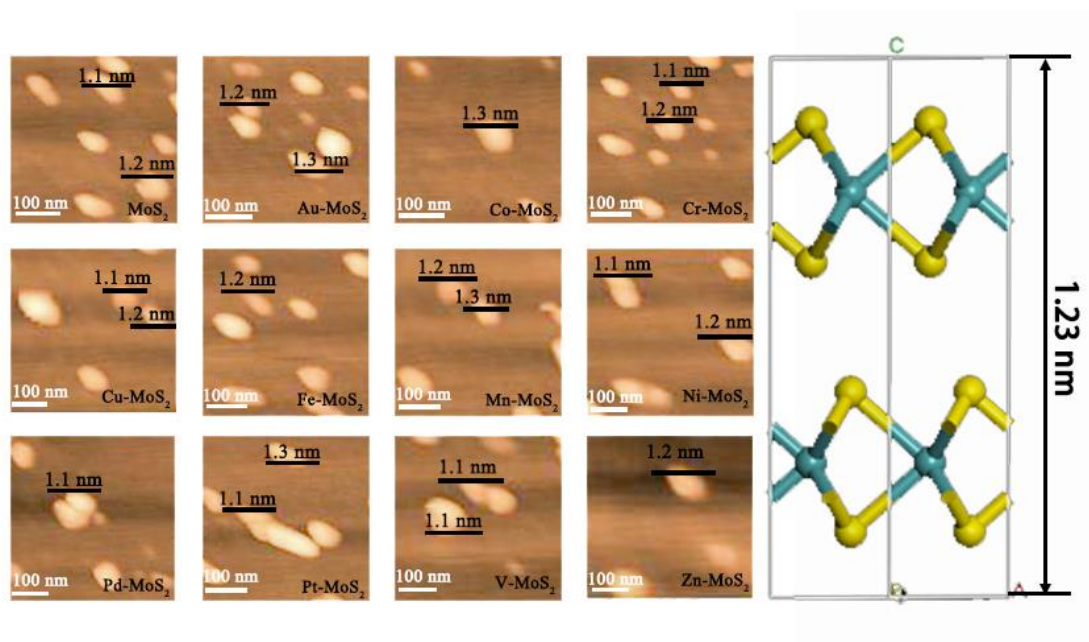


Figure S8. AFM images of different M-UMONs (Related to Figure 1). The right side shows theoretical thickness of MoS₂ nanosheet with two molecular layers. The AFM images indicates a uniform thickness of 1.2 nm, which corresponds to the two MoS₂ molecular layers.

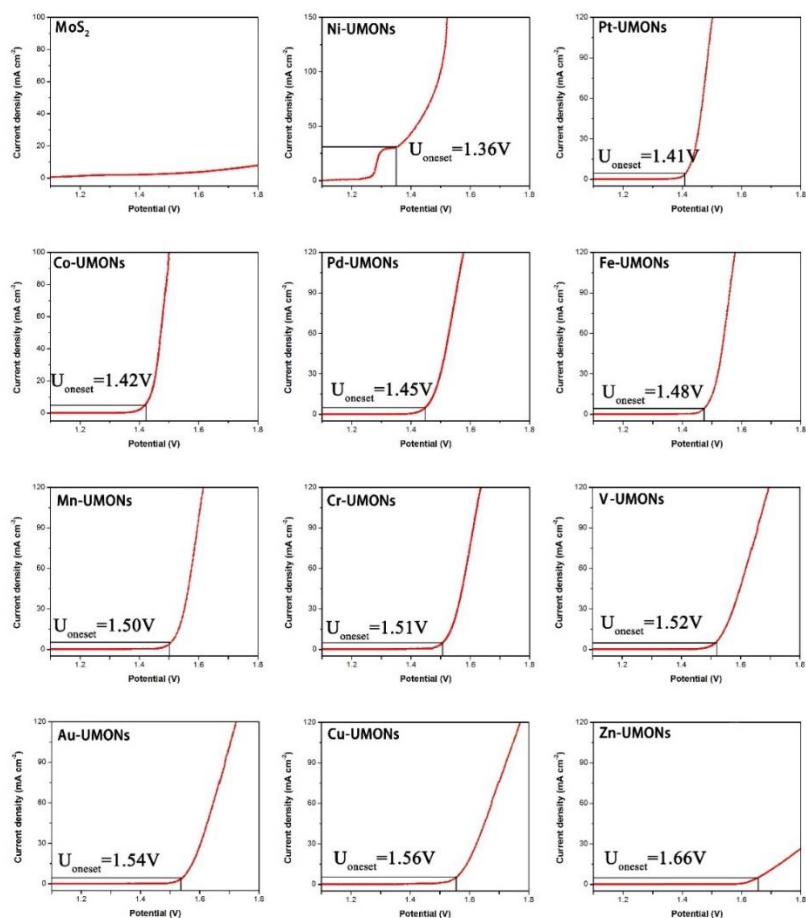


Figure S9. LSV curves of MoS₂ nanosheets and different kinds of M-UMONs (Related to Figure 4). The onset potential was defined as the potential at the current density of 5 mA cm⁻². The peak in 1.30 V ~ 1.35 V should be attributed to the oxidation of Ni (Zhao et al., 2016), and then the onset potential of Ni-UMONs were roughly estimated at 1.36V. The redox potentials of other transition metal elements were not in this potential range, so no oxidation peak were observed during the electrochemical measurements. The negligible current of MoS₂ nanosheets confirmed that the surface transition metal atoms are the main active sites, that is to say, the active sites are usually at the edge of the 2D materials (Friebel et al., 2015). However, in this work, pure MoS₂ nanosheets could offer negligible OER activity, when the single metal atoms were supported on the surface of MoS₂ nanosheet, the significantly enhanced OER performance was observed. These results showed the OER activity was mainly from the supported single metal atoms rather than the edge defect sites, confirming our frontier orbitals calculation results. Besides, the experimental results matches well with the theoretical overpotentials, validating our high-throughput calculation results of theoretical overpotentials.

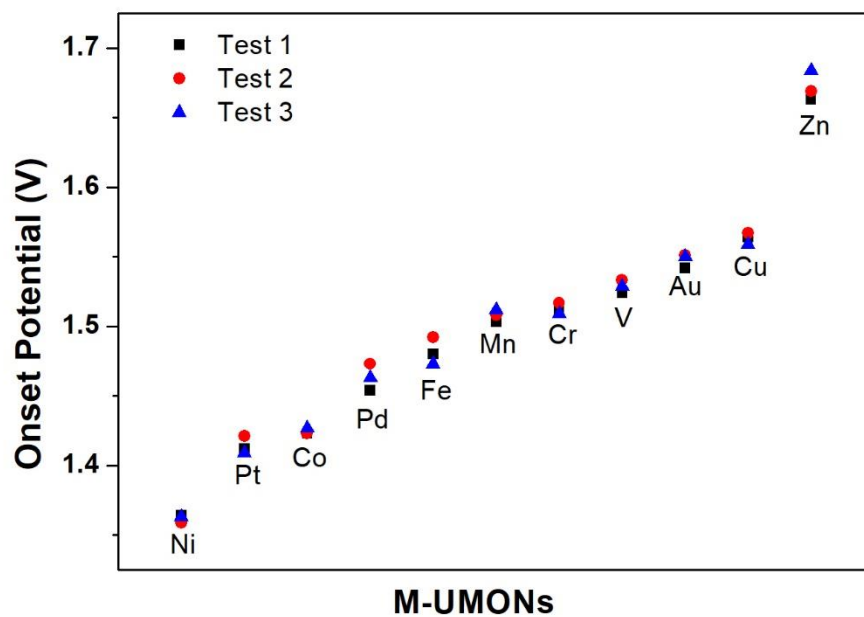


Figure S10. The onset potential of different kinds of M-UMONs in three parallel tests (Related to Figure 4). These results indicate that

our experimental results were credible, and no obvious differences were observed between these parallel tests.

Sc 0.94	Ti 0.89	V 0.81	Cr 0.91	Mn 0.92	Fe 0.81	Co 0.80	Ni 0.92	Cu 0.88	Zn 0.87
Y 0.95	Zr 0.80	Nb 0.82	Mo 0.95	Tc 0.80	Ru 0.87	Rh 0.94	Pd 0.93	Ag 0.89	Cd 0.89
La No Data	Hf 0.82	Ta 0.80	W 0.85	Re 0.84	Os 0.85	Ir 0.88	Pt 0.92	Au 0.91	Hg 0.89

Figure S11. M-S bond orders of different kinds of M-UMONs (Related to Figure 2, 3 and 4). The M-S bond orders values are displayed below the associated element symbol.

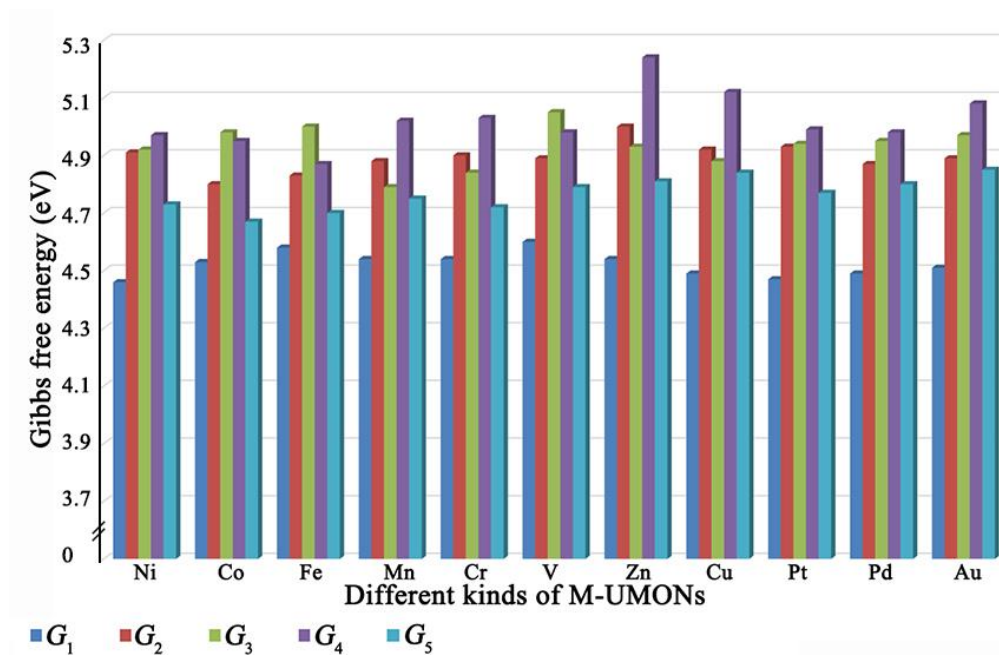


Figure S12 Gibbs free energy diagram of the OER process of above mentioned eleven kinds of M-UMONs (Related to Figure 4).

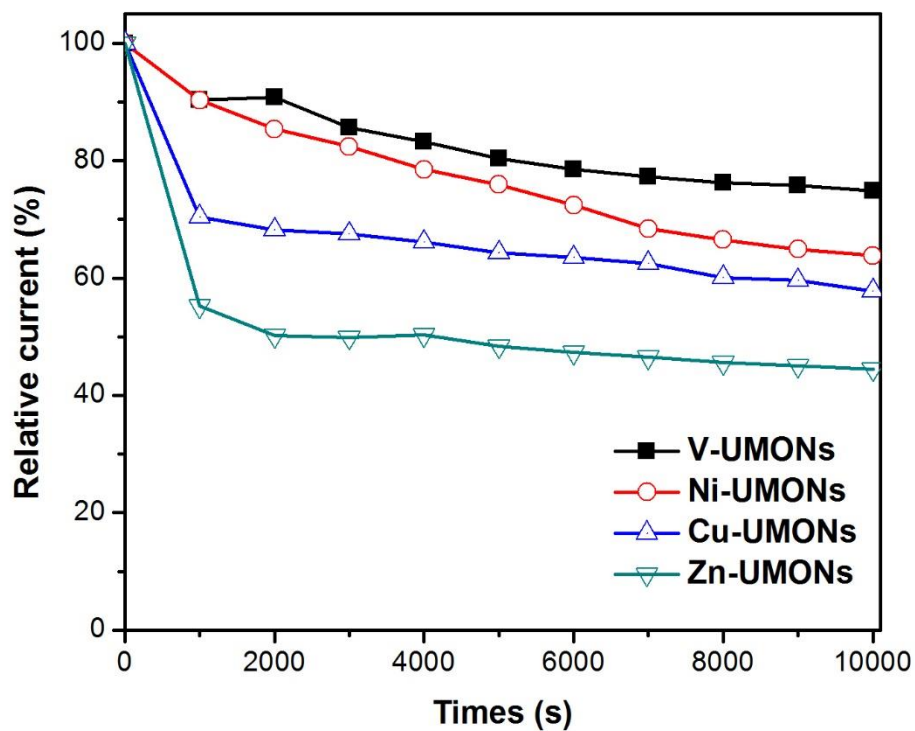


Figure S13. Chronoamperometric curves of V-UMONs, Ni-UMONs, Cu-UMONs and Zn-UMONs at the overpotential of 0.4 V (Related to Figure 3 and 4). These results indicated the tendency of catalysts stability is consistent with that of the M-S bond orders, which confirms our bond population calculations is rational.

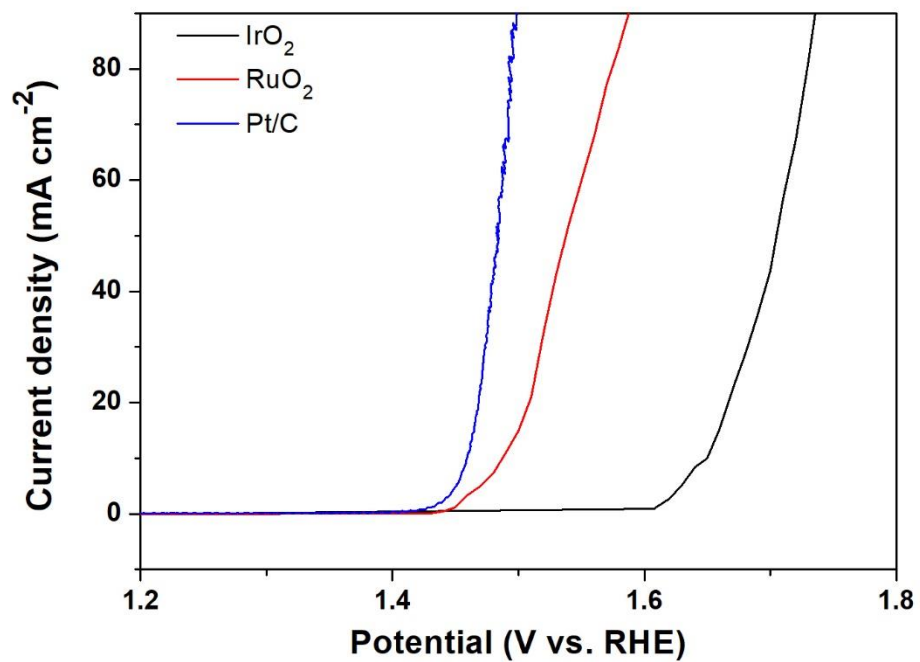


Figure S14. The LSV curves of commonly used OER catalysts including IrO₂, RuO₂ and Pt/C (Related to Figure 4 and S9). These results indicate that Ni-UMONs, Co-UMONs and Pt-UMONs could offer comparable performance and even outperform these commonly used OER catalysts. These results also confirmed construction of M-UMONs is a practical pathway to develop high-performance OER catalysts.

Supplemental Tables

Items	Mo-top site ^a	S-top site	Cav-site
Ni-MoS ₂	0	1.25	0.42
Co-MoS ₂	0	1.55	0.46
Fe-MoS ₂	0	0.94	0.24
Mn-MoS ₂	0	0.38	0.24
Cr-MoS ₂	0	0.41	0.14
V-MoS ₂	0	0.86	0.44
Zn-MoS ₂	0	0.39	0.02
Cu-MoS ₂	0	0.36	0.07
Pd-MoS ₂	0	0.14	0.14
Pt-MoS ₂	0	0.06	0.33
Au-MoS ₂	0	0.27	0.04

Table S1. Relative energy (eV) of different transition metal atoms binding configurations (Related to Figure 1).

^aThe energy of Mo-top configuration is used as reference.

Items	Transition metal	Mo	S	M(at%)
Ni-MoS ₂	1.57	58.21	40.22	4.29
Co-MoS ₂	1.63	59.32	39.05	4.43
Fe-MoS ₂	1.51	59.18	39.31	4.33
Mn-MoS ₂	1.47	59.56	38.97	4.28
Cr-MoS ₂	1.37	60.27	38.36	4.22
V-MoS ₂	1.42	59.42	39.16	4.46
Zn-MoS ₂	1.31	59.27	39.42	3.21
Cu-MoS ₂	1.54	59.09	39.37	3.88
Pd-MoS ₂	1.53	59.71	38.76	2.30
Pt-MoS ₂	1.82	60.03	38.15	1.49
Au-MoS ₂	1.48	59.20	39.32	1.20

Table S2. ICP-MS results (wt %) and derived atomic percentage (at%) of transition metal atoms of different kinds of M-UMONs (Related to Figure 1).

M-UMONs	Basis set	Mayer Bond Orders
Ni-S	DNP	0.8428/0.8712/0.8501
	DND	0.8419/0.8709/0.8505
Co-S	DNP	0.8696/0.9351/0.8679
	DND	0.8699/0.9350/0.8676
Fe-S	DNP	0.8847/0.9938/0.8859
	DND	0.8841/0.9935/0.8853
Mn-S	DNP	0.7724/0.8193/0.7691
	DND	0.7723/0.8190/0.7689
Cr-S	DNP	0.7582/0.7794/0.7577
	DND	0.7584/0.7791/0.7576

Table S3. The calculated Mayer bond orders with different basis set (Related to Figure 2 and 3). This result showed that Mayer bond

order is almost keep unchanged when the basis set changed.

Supplemental References

- Mayer, I. (1986). Bond orders and valences from ab initio wave functions. *Int. J. Quantum Chem.* *29*, 477-483.
- Torres, J. A., Santiago, L. R., Sodupe, M. and Rauk, A. (2011). Structures and stabilities of Fe^{2+/3+} complexes relevant to alzheimer's disease: an ab initio study. *J. Phys. Chem. A* *115*, 12523-12530.
- Liu, G., Robertson, A. W., Li, M. M.-J., Kuo, W. C. H., Darby, M. T., Muhieddine, M. H., Lin, Y.-C., Suenaga, K., Stamatakis, M., Warner, J. H., and Tsang, S. C. E. (2017). MoS₂ monolayer catalyst doped with isolated Co atoms for the hydrodeoxygenation reaction. *Nat. chem.* *9*, 810-816.
- Stevens, M. B., Enman, L. J., Batchellor, A. S., Cosby, M. R., Vise, A. E., Trang, C. D. M., and Boettcher, S. W. (2017). Measurement techniques for the study of thin film heterogeneous water oxidation electrocatalysts. *Chem. Mater.* *29*, 120-140.
- Zhuang, Z., Sheng, W., and Yan, Y. (2014). Synthesis of monodisperse Au@Co₃O₄ core-shell nanocrystals and their enhanced catalytic activity for oxygen evolution reaction. *Adv. Mater.* *26*, 3950-3955.
- Chattaraj, P. K., Maiti, B., and Sarkar, U. (2003). Philicity: a unified treatment of chemical reactivity and selectivity. *J. Phys. Chem. A* *107*, 4973-4975.
- Mavrikakis, M., Hammer, B., and Nørskov, J. K. (1998). *Phys. Rev. Lett.* *81*, 2819-2822.
- Zhao, S., Wang, Y., Dong, J., He, C.-T., Yin, H., An, P., Zhao, K., Zhang, X., Gao, C., Zhang, L., Lv, J., Wang, J., Zhang, J., Khattak, A. M., Khan, N. A., Wei, Z., Zhang, J., Liu, S., Zhao, H., and Tang, Z. (2016). Ultrathin metal-organic framework nanosheets for electrocatalytic oxygen evolution. *Nat. Energy* *1*, 16184.
- Zhao, S., Wang, Y., Dong, J., He, C.-T., Yin, H., An, P., Zhao, K., Zhang, X., Gao, C., Zhang, L., Lv, J., Wang, J., Zhang, J., Khattak, A. M., Khan, N. A., Wei, Z., Zhang, J., Liu, S., Zhao, H., and Tang, Z. (2016). Ultrathin metal-organic framework nanosheets for electrocatalytic oxygen evolution. *Nat. Energy* *1*, 16184.
- Friebel, D., Louie, M. W., Bajdich, M., Sanwald, K. E., Cai, Y., Wise, A. M., Cheng, M.-J., Sokaras, D., Weng, T.-C., Alonso-Mori, R., Davis, R. C., Bargar, J. R., Nørskov, J. K., Nilsson, A., Bell, A. T. (2015). Identification of Highly Active Fe Sites in (Ni,Fe)OOH for Electrocatalytic Water Splitting. *J. Am. Chem. Soc.* *137*, 1305-1313.

